Studying the deployment of high-lift devices by using dynamic Immersed Boundaries

Francesco Capizzano

Centro Italiano Ricerche Aerospaziali, Via Maiorise, 81043 Capua, Italy.

E-mail: f.capizzano@cira.it

Triyantono Sucipto

IBK Innovation GmbH & Co. KG, Butendeichsweg 2, 21129 Hamburg, Germany

E-mail: Triyantono.Sucipto@ibk-innovation.de

Abstract.

Purpose - The paper describes a research effort towards the comprehension of the unsteady phenomena due to the deployment of high-lift devices at approach/landing conditions.

Design/methodology/approach - The work starts from a preexisting platform based on an Immersed Boundary (IB) method whose capabilities are extended to study compressible and viscous flows around moving/deforming objects. A hybrid Lagrangian-Eulerian approach is designed to consider the motion of multiple bodies through a fixed Cartesian mesh. That is, the cells' volumes do not move in space but rather they observe the solid walls crossing themselves. A dynamic discrete forcing makes use of a moving least-square procedure (MLSQ) which has been validated by simulating well-known benchmarks available for rigid body motions. Partitioned FSI strategies are explored to consider aeroelastic phenomena. A shared platform, between the aerodynamic and structural solvers, fulfils the loads' transfer and drives the sequence of operating steps.

Findings - The first part of the results is devoted to a basic $2D$ study aiming at evaluating the accuracy of the method when simple rigid motions are prescribed. Afterwards, the paper discusses the solution obtained when applying the dynamic IB method to the rigid deployment of a Krueger-flap. The final section discusses the aeroelastic behaviour of a three-element airfoil during its deployment phase. A loose FSI coupling is applied for estimating the possible loads' downgrade.

Practical implications - The proposed method improves automation in FSI numerical analysis and relaxes the human expertise/effort for meshing the computational domain around complex three-dimensional geometries. The logical consequence is an overall speed-up of the simulation process.

Originality/value - The value of the paper consists in demonstrating the applicability of dynamic IB techniques for studying high-lift devices. In particular, the proposed Cartesian method does not want to compete with body-conforming ones whose accuracy remains generally superior. Rather, the merit of this research is to propose a fast and automatic simulation system as a viable alternative to classic multi-block structured, chimera or unstructured tools.

Keywords: *Compressible Fluids, Finite-Volume method, Immersed Boundary, Mesh adaptation, High-lift device, FSI*

Paper type: *Research paper.*

1. Introduction

Immersed boundary (IB) methods represents a sounding and credibly way forward for studying unsteady flows around complex geometries with moving/deforming surfaces. Although, body-conforming methods have successfully applied to moving-boundary problems[1, 2, 3, 4] their applicability to three-dimensional configurations with complex kinematics is not completely satisfactory and often computationally expensive.

Indeed, almost all block-structured and unstructured methods use re-meshing or mesh-deformation techniques to follow Lagrangian surfaces. Apart from the huge programming effort, these methods implies a high turn-around time and often the downgrade of the mesh quality due to mesh stretching. When large displacements occur, for example, a moving-mesh technique generates highly skewed and/or degenerate cells (zero or negative volumes).

Sliding-mesh or re-meshing procedures can alleviate these issues but are time-consuming[5]. In particular, some block-structured techniques are hardly applicable in case of geometries with very small gaps such as the ones occurring at the wing-cuts along the span between the main the flap and the aileron components.

Overset multi-block techniques avoid re-meshing or mesh-deformations even if they are formally non-conservative and not prone towards mesh automation.[6, 7, 4]

On the contrary, Cartesian methods exploit the advantages of fast and automatic pre-processing with the flexibility of transient mesh adaptations[8, 9, 10]. Rigid body motions[11, 12] (RBM) or fluid-structure interactions[11, 13, 14] (FSI) are often obtained by moving objects through a fixed Cartesian mesh. This implies that cells emerge from the solid towards the fluid region and vice-versa. As darkening cells are simply switched off, the 'fresh-cleared' ones should participate to the new flow state. However, they do not have a valid time-history from previous time-steps. Then, reconstructions in both space and time are usually carried out but at the cost of generating local as well as global conservation errors. The latter, if not catastrophic, cause spurious forces' oscillations (SFOs).

Among Cartesian methods, the cut-cell ones deserve to be mentioned due to their conservative properties at wall. Anyhow, the modifications to the spatial scheme at cut-cells facing the geometry boundaries cause local numerical noise as well. The use of redistribution weights made by Schneiders et al. [14] is able of relaxing the issue.

Analogously, many IB techniques add proper body forces in the governing equations and make use of analytic delta functions that can be manipulated to smooth transient oscillations[15, 10]. Alternatively, sharp-interface IB methods apply discrete body forces

which satisfy wall BCs but violate local conservation[8, 16].

A 'field-extension' technique is proposed by Yang and Balaras[17] that extrapolate quantities to solid nodes at each time-step. This procedure reconstructs the flow field in those cells that will emerge towards the fluid region at the next time-step.

A moving least-square procedure (MLSQ) for incompressible methods is proposed by Vanella et al.[11]. They use a smooth discrete forcing that guarantees momentum conservation between Lagrangian and Eulerian meshes.

The paper discusses the development and validation of a fast and automatic IB method for unsteady flows around moving/deforming objects. A hybrid Lagrangian-Eulerian approach allows the motion of arbitrary objects through a fixed Cartesian grid. A dynamic adaptive mesh refinement (AMR) procedure is developed in proximity of moving walls. A smooth discrete forcing is obtained by a moving least-square procedure (MLSQ)[11, 13] with the aim of guaranteeing a consistent and accurate loads' transfer between the Lagrangian and Eulerian markers.

The proposed IB tool has been validated on some benchmarks dealing with rigid body motions (RBM). Here, for brevity, we discuss only the results for a transonic inviscid flow around an oscillating airfoil and compare them with other data from the literature.

A first application examines the solution obtained when applying the dynamic IB-method to the rigid deployment of a Krueger-flap. This represents a challenging application due to the high rotation-speed. The latter may cause robustness issues for many body-conforming as well as Cartesian methods. Indeed, large displacements occur and local time-step restrictions are needed to avoid numerical instabilities. In particular, the relative motion between the Krueger-plate and bull-nose causes small gaps during the deployment/retraction phases that may impair the convergence process (flow through a narrow area). Even the progressive approaching between the two surfaces towards the complete merging (fully-deployed configuration) represents an issue for body-conforming approaches and an open-field of research.[4]

The present research is also exploring different fluid-structure interaction (FSI) strategies for driving the solution sequence appropriately. These are based on a partitioned coupling between the present IB method and a FEM-solver. The latter communicate each other by means of a proper interface to allow conservative loads' mapping between computational fluid dynamics (CFD) and computational structural mechanics (CSM) meshes.

In particular, a loose two-way coupling is set-up which uses time-accurate aerodynamic loads to compute linear and static deformations in a very fast way. Of course, the deformation velocities are zero. Then, the modified shape is used to compute the flow-state at the next time-step. An implicit loop drives the codes to loads' convergence. This coupling is applied to study the aeroelastic behaviour of a slat-main-flap device during its deployment phase.

2. Numerical background

The present research starts from an unstructured IB framework specifically developed to speed up and automate as much as possible the simulation of unsteady viscous flows around stationary configurations[18, 19]. The governing equations are the three-dimensional unsteady compressible Navier-Stokes (NaS) whose basic conservative variables are the density, the mass flux vector and the total energy per unit volume $(\rho, \rho u, \rho v, \rho w, \rho E)$. The unsteady RANS model is currently applied to solve turbulent flows. In addition, a hybrid RANS-LES model is available whose formulation is proposed by Kok[20] with the name of eXtra Large Eddy (XLES). It relies on the composition of a k-equation SGS model and the $k-\omega$ TNT one[21].

The Cartesian method applies a finite volume (FV) approximation to solve the differential equations on locally refined meshes. A 2^{nd} order space-centered scheme (CDS) is applied based on skew-symmetric convective fluxes[20]. The viscous fluxes of NaS equations are spatially discretized by averaging the gradients at the neighbouring cell centers and applying a proper correction in the direction connecting the cell-centers[22, 23].

An implicit 2^{nd} order dual-time-stepping (DTS) technique integrates equation in the time domain[24, 25]. A low-storage Runge-Kutta relaxation advances the discrete equations in the dual-time[25] and a 1^{st} order prediction formula speeds-up the pseudo-time integration.

A collection of sharp and discrete body forces mimics the effects of steady walls on the surrounding flow. Instead of adding these source terms into the momentum equations, the present method modifies the basic FV scheme near the wall by satisfying proper *BC*s de-facto generating the proper forcing in an indirect way. For example, consider the simplified sketch shown in figure 1 where the Cartesian cells (black-colored) are cut by the wall-surface (red-colored). Proper fluxes are forced at the near-wall *IB-faces* (blue-colored circles) to satisfy the desired Dirichlet/Neumann conditions at the wall.

In this case, we speak of a *face-based* approach whose main advantage is applying the same FV scheme on both the far- and near-wall cells. Especially the latter require a proper treatment. In particular, we need to estimate the flow state vector $\mathbf{Q}$ at their *IB-face* centers. To do that, an *inner-layer* is built up by setting an ensemble of fictitious forcing points F_i (green-colored circles) at a fixed perpendicular distance δ^F from the wall. Here, the distance δ^F is set to $O(\Delta x_i)$ where Δx_i is the smallest cell spacing. Each flow-state vector Q_i is there reconstructed from the neighbouring cells by using a weighted least-square procedure (WLSQ). The *IB-face* center values can be adapted to satisfy the desired wall BCs once known the Q_i at the forcing point[26]. The way the generic convective or diffusive fluxes are computed depends on the flow regime.

In case of Euler flows a linear interpolation is coupled with classic slip-wall BCs to obtain feasible values at face-centers[27, 28]. No-slip wall and other *Low-Reynolds* BCs are applied for laminar flows. Linear interpolators, however, have sense for 2^{nd}

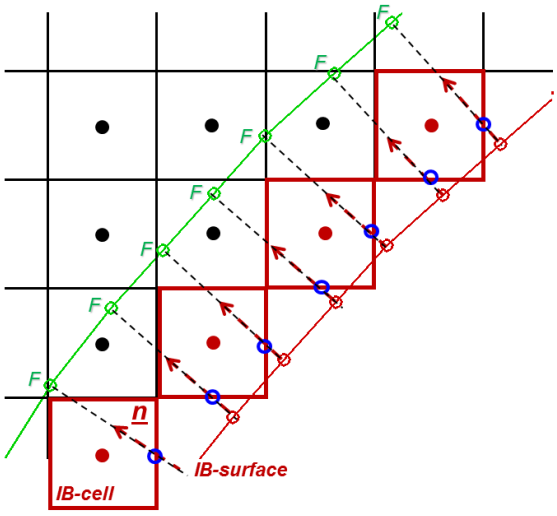

Figure 1. Sharp discrete-forcing.

order solvers provided that a sufficient mesh refinement is guaranteed in proximity of the wall[29, 30].

At high Reynolds numbers, the solver uses a wall-model to mimic the non-linearities of turbulent boundary-layers. A virtual sub-grid zone is solved by means of simplified thin boundary layer PDEs. Upper BCs get information from the surrounding external flow and wall BCs drive the non-linear solution down to the wall. More details can be found in Refs. [26, 31].

3. Dynamic immersed boundaries

The modelling of a Lagrangian body that moves through a Eulerian domain poses different issues: the tracking of moving surfaces, a dynamic meshing, the stability and accuracy of the schemes. The former aspects are addressed by exploiting the pre-existing simulation framework based on ray-tracing techniques as well as fast and automated meshing.

The major difficulty lies in the rising and fading of fluid cells around moving walls. The literature on the IB topic have experienced spurious oscillations (SFOs) in transient loads which are due to lack of local mass conservation and changes of the discrete operators near the wall. In particular, Leo et al.[32] and Seo et al.[33] ascribe spatial and temporal discontinuities to 'fresh-cleared' and 'dead' cells. Their numerical experiments show that pressure oscillations scale as $(\Delta x_j)^2/(\Delta t)$ and $(\Delta x_j)^3/(\Delta t)$ in two- and three-dimensions respectively[33].

A way of mitigating SFOs is to adopt a discrete forcing based on a moving least-square (MLSQ) procedure. In particular, the MLSQ proposed by Vanella et al. [11] and De Tullio et al.[13] builds up a smooth discrete forcing on the Lagrangian surface and satisfies local wall BCs. Then the procedure converts the Lagrangian forcing back

to the Eulerian mesh provided that the force acting on the fluid is not changed by the transfer. However, their work is focused on incompressible methods.

Here a similar procedure is adopted but applied to compressible fluids. In particular, the IB surfaces are allowed to move less than one IB-cell size at each time-step thus imposing $CFL_{body} = U_{body}\Delta t/\Delta x < 1$. The violation of this constraint would impair the explicit character of the method. Extensions to implicit body motions for Cartesian methods are discussed in Murman et al.[34].

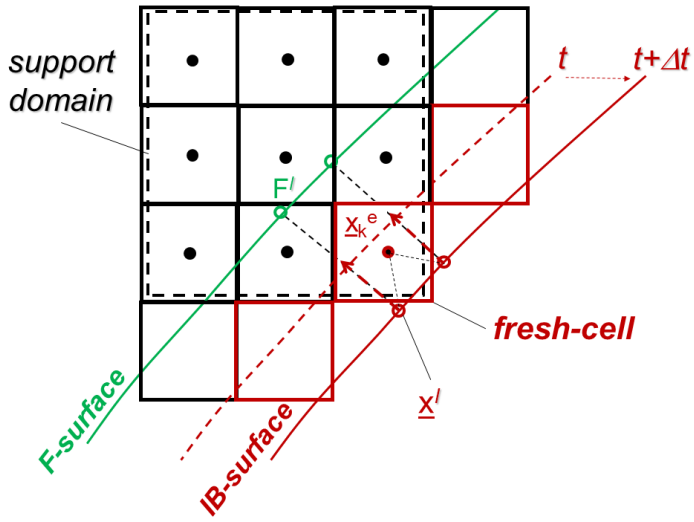

Figure 2. Emerging cells and simplified view of MLSQ procedure.

The MLSQ approach is organized so as to exploit the framework previously developed for static boundaries. The draft shown in figure 2 represents a boundary moving between the two instants t^n and t^{n+1}. The emerging 'fresh' cell (red colored) represents the target Eulerian marker whose flow-state $\mathbf{Q}_k^n$ has to be reconstructed somehow by using fluid neighbours. The latter are chosen among the ones hosted by a 'support domain' spanning three cell-size in each Cartesian direction (the black-dashed volume). Note that, the support domain contains one or more forcing-points (green open-circles) conjugated with wall Lagrangian markers (red open circles) according to the geometric arrangement described for steady boundaries. The role of forcing points is to modify the $\mathbf{Q}^l$ vector at Lagrangian markers so as to satisfy wall BCs.

The Eulerian markers in the support domain give a discrete representation of each flow quantity $\varphi(x, y, z)$. They are used to search for an approximating linear function in the LSQ sense and having the form

$$f(x, y, z) = b_0 + b_1 x + b_2 y + b_3 z = \sum_{i=0}^{3} \psi_i b_i = \Psi^T \mathbf{b} \tag{1}$$

where $\Psi^T = [1, x, y, z]$ is a basis vector and $\mathbf{b}$ is the vector whose components are the coefficients of the linear function. The values of the four unknowns b_i are obtained by

minimizing the following functional

$$G(f) = G(b_0, b_1, b_2, b_3) = \sum_{k=1}^{N_e} w_k \left[f(\mathbf{x}_k) - \varphi(\mathbf{x}_k) \right]^2 \tag{2}$$

where N_e is the total number of Eulerian markers belonging to the support domain and w_k is a weighting function depending on the distance between the target point and the *k-th* cell-center $\mathbf{x}_k$. Here we use exponential weighting function[13]

$$w_k = \begin{cases} e^{(r_k/\varepsilon)^2} & r_k \leq 1 \\ 0 & r_k > 1 \end{cases}$$

where $\varepsilon = 0.3$ and r_k is defined as

$$r_k = \frac{|\mathbf{x} - \mathbf{x}_k|}{r_i}$$

with r_i the size of the support domain in the $i-th$ direction. Setting the derivatives $\partial G/\partial b_i$ equal to zero, the following system of equations is obtained

$$\sum_{j=0}^{3} A_{ij} b_j - c_i = 0 \quad i = 0, ..., 3 \tag{3}$$

where the matrix A_{ij} is defined as

$$A_{ij} = \sum_{n=1}^{N_e} w_n \; \psi_i(\mathbf{x}_k) \; \psi_j(\mathbf{x}_k) \tag{4}$$

and the known terms are

$$c_i = \sum_{k=1}^{N_e} w_k \; \psi_i(\mathbf{x}_k) \; \phi(\mathbf{x}_k) \tag{5}$$

Finally the coefficients of the linear function can be computed by inverting the matrix A_{ij} and the flow state at the *l-th* forcing point is approximated as

$$\mathbf{Q}^{F^l} = \sum_{k=1}^{N_e} \phi_k^l \mathbf{Q}^k \tag{6}$$

where ϕ_k^l are the shape functions at the forcing point $\mathbf{x}^{F^l}$ conjugated with the wall Lagrangian marker $\mathbf{x}^l$. By construction, the support domain guarantees 8 and 26 Eulerian markers in two- and three-dimensions respectively. Once known $\mathbf{Q}^{F^l}$, the flow state $\mathbf{Q}^l$ at wall $\mathbf{x}^l$ is computed so as to satisfy the prescribed BCs

$$\mathbf{Q}^l = \mathbf{Q}(\mathbf{x}^{F^l}, \mathbf{x}_w^l) \tag{7}$$

Besides, for a moving body its velocity $\mathbf{U}^l_{body}$ must be considered

$$\mathbf{U}^l = \mathbf{U}^l_w - \mathbf{U}^l_{body} \tag{8}$$

In particular, the no-slip velocity BC becomes the velocity of the wall

$$\mathbf{U}^l = 0 \qquad \Rightarrow \qquad \mathbf{U}^l_w = \mathbf{U}^l_{body}$$

In case of slip velocity, the non-penetration condition prescribes that the normal component of the wall velocity matches the surface one

$$\mathbf{U}^l \cdot \mathbf{n} = 0 \qquad \Rightarrow \qquad U^l_n = \left(U^l_n\right)_{body}$$

Finally, the same shape functions used for the WLSQ at forcing points are applied to transfer back the flow states from the N_l Lagrangian markers (two markers in the example of figure 2) to the center of the target 'fresh' cell

$$\mathbf{Q}^e_k = \sum_{l=1}^{N_l} \phi^l_k \mathbf{Q}^l \tag{9}$$

The described MLSQ procedure falls into the family of dynamic 'reconstruction' methods and is very similar to one discussed in Refs.[11, 13]. Note that, the AMR technique is applied at each time-step thus allowing a transient mesh adaptation.

4. FSI coupling strategies

This section describes the procedure for coupling the dynamic IB method with the Nastran structural solver following the partitioned approach shown in figure 3. Consider the motion of an object moving into an unsteady flow field. At each time step $t+\Delta t$ the pre-processor tags the mutual position of moving surfaces with respect to the fixed cells. After the loads' transfer, the structural solver computes the new shapes and the cycle restarts. The surface deformations can be computed at each or every 'N' time-steps depending on the coupling approach.

A key aspect is the design of a proper interface to allow the loads' mapping and the communications between solvers. Usually the aerodynamic mesh is more refined than the structural one. The use of non-conservative interpolators introduces errors that could potentially impair the entire transient process. Here, the loads' transfer is based on a robust and consistent Radial-Basis-Function (RBF) which allows minimizing the errors due to countless data exchange[35].

An implicit loop is fundamental to drive both codes towards converging solutions at each time-step. The process uses convergence criteria based on both loads' and displacements' errors. Usually, three to five implicit iterations suffice even if a limiting number of iterations is recommended. Indeed, though mesh interpolators are designed

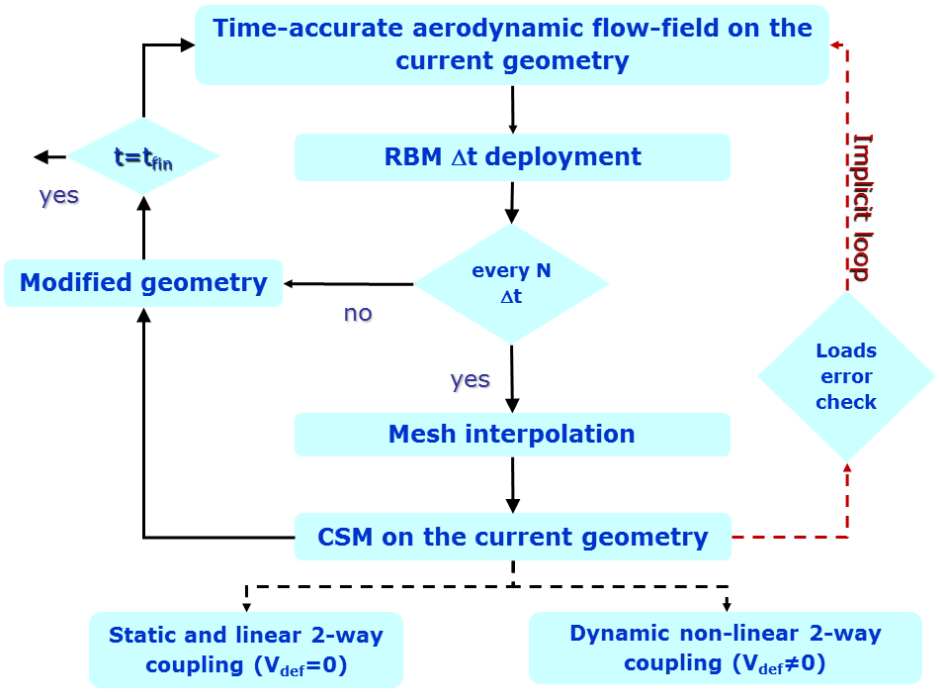

Figure 3. Partitioned coupling strategies.

to be energy conserving, errors due to the partitioned and/or the staggered nature of the coupling can drive the entire process to diverge.

In general, loose and tight 'two-way' couplings are possible. Here, we consider loops based on time-accurate aerodynamics and steady-linear or dynamic non-linear structural analyses.

A 'static two-way FSI-coupling' provides a loose interaction between computational fluid dynamics (CFD) and computational structural mechanics (CSM). Here we apply the staggered scheme shown in figure 4 with data-exchange every Δt_{FSI}. In particular, CFD starts its computation at t^i_{CFD} and delivers the surface loads $\mathbf{f}_i$ to CSM. The interface makes data interpolation, mapping and loads transfer. The structural solver applies linear and static assumption with stiffness S_i and delivers the modified surfaces to CFD. The displacements $\mathbf{d}_i$ are transferred back to CFD for the next time-step. The deformation velocities are not considered. An implicit loop drives the codes to loads' convergence. Due to the use of steady CSM modelling, the FSI loop is driven by the unsteady CFD process that runs a number of physical $\Delta t_{CFD} = \Delta t_{FSI}$ time-steps. In particular, the loose coupling is applied to compute the aeroelastic loads due to the slat-main-flap airfoil deployment as described in the results' section.

The FSI interface is further updating to allow a 'dynamic two-way coupling'. The latter consists of a staggered scheme with data-exchange every Δt_{FSI} as shown in figure 5. In particular, CFD starts its unsteady computation at $t^j_{CFD} = t^i_{FSI}$. The interface makes data interpolation, mapping and delivers the surface loads f_i to CSM. The latter accounts for the dynamic behavior of the structure by means of a transient

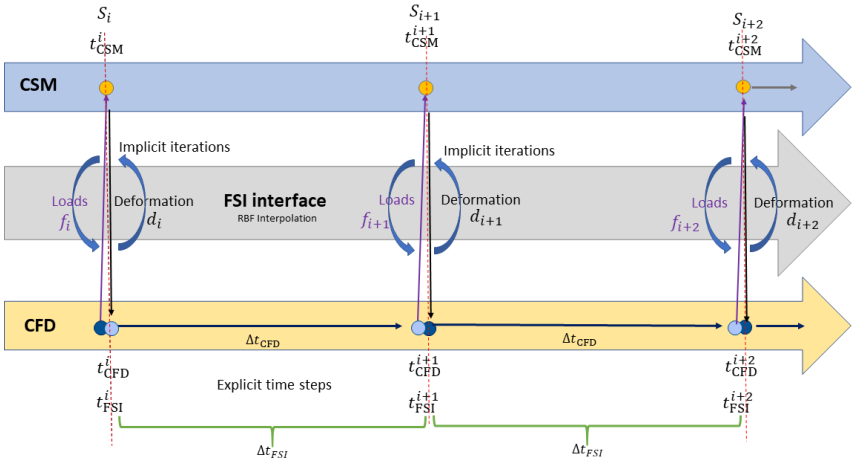

Figure 4. FSI simulation strategy: static two-way coupling.

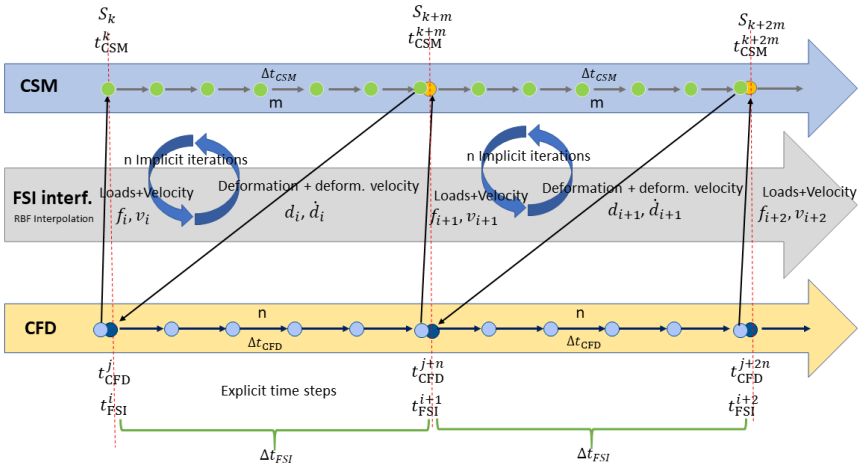

Figure 5. FSI simulation strategy: dynamic two-way coupling

solver. However, the deformations are kept small so that the linearity of the structure plays. The Nastran tool computes the structural model with stiffness S_k by explicitly computing M sub-steps Δt^k_{CSM} covering the entire Δt_{FSI}. Surface deformations $\mathbf{d}_i$ and deformation velocities $\dot{\mathbf{d}}_i$ are transferred back to CFD. An implicit loop guarantees loads' convergence.

This strategy pre-requisites small Δt_{FSI} to keep the structure linearity. Besides, a small time-step justifies time-back from CSM to CFD. In general, the choice of the Δt_{FSI} is an issue for partitioned approaches as it represents a compromise between stability, robustness and computational resources. For example, choosing $\Delta t_{FSI} = \Delta t_{CSM}$ could catastrophically increase the computational time. Alternatively, the CSM could be applied every $N \cdot \Delta t_{CFD}$ time-steps and in this case $\Delta t_{FSI} = N \cdot \Delta t_{CFD}$.

Note that, the dynamic coupling is still under development. If successful, it will be

applied to study the aeroelastic loads during a Krueger-flap deployment.

5. Results

The following sections discusses the numerical results obtained by using the dynamic IB-method described above. Classic far-field boundary conditions, based on the characteristic's theory, are used. For turbulent cases, the $k-\omega$ closure is applied to the RANS equations. The wall-model is activated at solid boundaries.

The results obtained for the pitching airfoil and the Krueger-flap deployment refer to the sole interaction of the external flow with imposed rigid motions. On the contrary, the section on the slat-main-flap deployment considers the rigid motions and the aeroelastic effects as well.

5.1. Pitching airfoil

A widely adopted benchmark for unsteady solvers is the AGARD $CT5$ transonic and inviscid flow around an oscillating $NACA0012$ airfoil. The latter rotates harmonically about the quarter-chord at $M = 0.755$, following the pitching law

$$\alpha(t) = \alpha_m + \alpha_0 sin(2\pi f^+ t^+) \tag{10}$$

where $f^+ = f\,c/U_\infty$ is the non-dimensional frequency based on the free-stream velocity and the airfoil chord length c. The reduced frequency is $k = \pi\, f^+ = 0.0814$ and the angle of incidence varies around $\alpha_m = 0.016°$ reaching a maximum of $\alpha_0 = 2.51°$. The computational domain spans $30c \times 30c$ away from the surface and consists of $48,760$ Cartesian cells with a minimum dimensionless size of $\Delta x^+ = 9.7656 \cdot 10^{-4}$. The periodic rotation causes the shock-buffeting on both the upper and the lower sides making the test challenging for any numerical scheme. In this case, we exploited the AMR strategy to follow pressure gradients accurately. Indeed, the resolution of these zones is crucial for computing accurate transient loads.

Time-accurate computations are carried out for 154.48 convective time-units (CTUs) by using two different time steps $T/360$ and $T/720$. The latter guarantee the CFL constraint $CFL_{body} < 1$ at trailing-edge and low levels of SFOs as shown in figure 6-a. The results are compared with body-conforming data[36] and experimental measurements[37] from literature. In particular, the figure 6-b shows an overall agreement between the numerical data. Anyway, both of them slightly underestimates the experiments. Regarding the accuracy, no significant differences are observed in the solution when using 360 or 720 steps per period.

Comparisons in terms of instantaneous Cp distributions are shown in figure 8. The plots contain the present results, the numerical data from Kirshman et al[38] and the experimental measurements at two different phases. In the first case $\phi = 67.8°$, the airfoil is near the maximum incidence $\alpha(t) = 2.34°$ and a shock acts on the upper surface. The present results agree with the solution of Kirshman et al. obtained by using a Cartesian

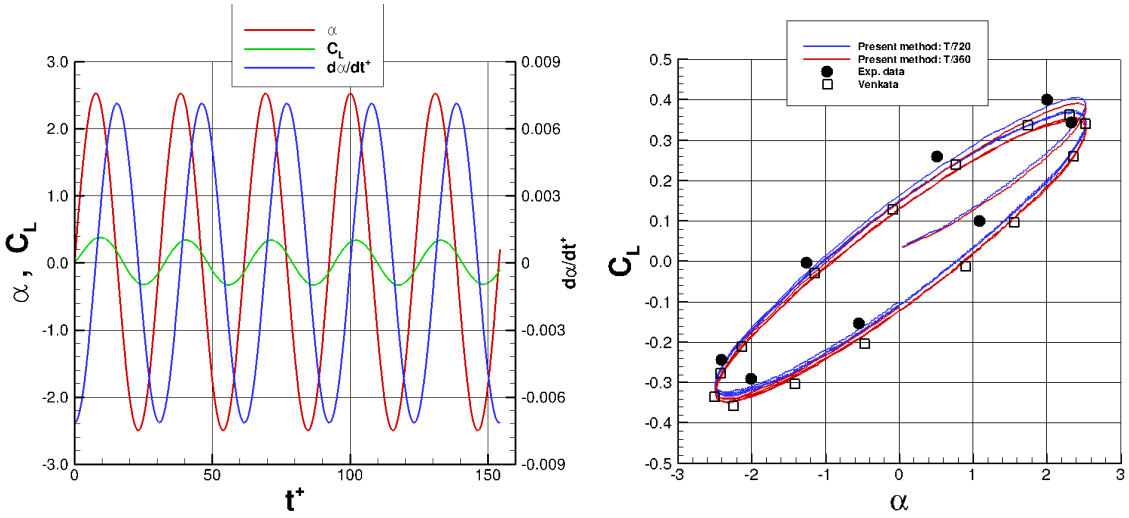

(a) Transient quantities. (b) Lift coeff.

Figure 6. *AGARD−TC*5 pitching airfoil: transient lift coeff. Present method (solid), body-conforming method[36] (□) and experiments[37] (•).

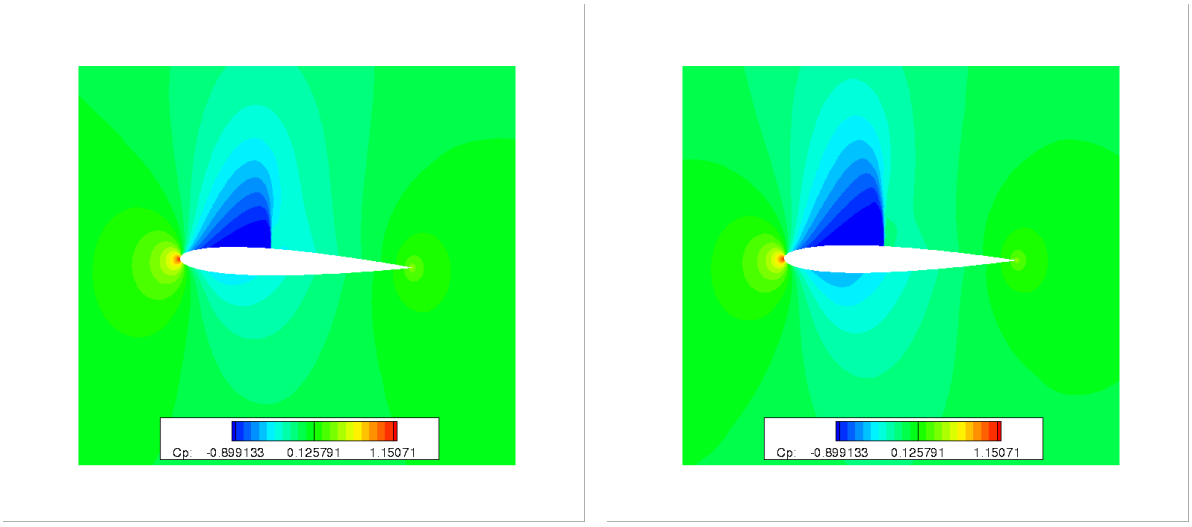

(a) $\alpha(t) = 2.34°$. (b) $\alpha(t) = -0.54°$.

Figure 7. *AGARD − TC*5 pitching airfoil: contour map of instantaneous pressure coeff.

method. Nevertheless, both numerical solutions locate the shock slightly upstream than the experimental measurements.

The second phase $\phi = 347.2°$ corresponds to $\alpha(t) = -0.54°$ when a stronger shock plays on the upper-side. Again, both numerical methods match the measured pressure levels on airfoil but they fail to capture the shock-wave position.

On the whole, these comparisons as well as the low levels of transient SFOs demonstrate the accuracy and robustness of the dynamic IB-method.

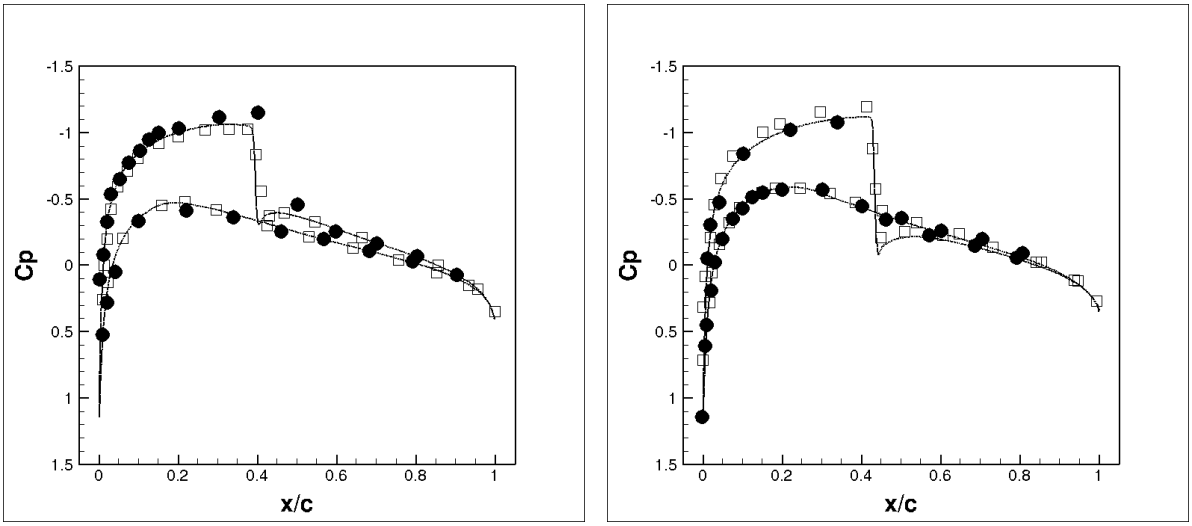

(a) $\alpha(t) = 2.34°$. (b) $\alpha(t) = -0.54°$.

Figure 8. $AGARD - TC5$ pitching airfoil: instantaneous pressure coeff. Present method (solid), Cartesian method[38] (□) and experiments[37] (•).

5.2. Krueger-flap deployment

The geometry is based on the DLR-F15 multi-element high-lift airfoil[39]. The geometry was modified by Dassault Aviation in the scope of JTI CleanSky-SFWA to reproduce the leading-edge shape of a natural laminar airfoil (NLF). First results using this geometry have been published in [40], which is the only publication that is mentioning this modification up to now. The airfoil consists of a main element incorporating the NLF leading edge and a flap, positioned at a rather swallow angle to avoid any risk of flap separation. The flap is fixed in its take-off position of $\theta = 13°$ and does not move during the Krueger deployment (see figure 9).

The Krueger device is composed of a Krueger-plate rotating around its hinge point and the bull-nose having its own motion. Note that, the two elements join only in the final phase and a small gap is present for large part of the deployment. That is, the air is obliged to flow through a narrow area during large part of the simulation. Numerical issues could potentially arise in this area. Instead of lowering the code performance (e.g. by limiting the time-step), the Krueger-plate and the bullet-nose are joined and the simulation is started from a partially rotated position of $\theta = 22.915°$ as shown in figure 10.

The design flow conditions are $Mach = 0.15$ and $Re_\infty = 2 \cdot 10^6$ based on the main element chord length of $c = 0.6\,m$. The multi-component airfoil is the section of a full-span model (zero swept angle) that will be object of wind-tunnel measurements in the short term. The suggested angle of incidence is $\alpha = 10°$.

The two-dimensional Cartesian mesh spans $30c \times 30c$ away from the surface and counts a variable number of $O(10^5)$ cells with a minimum cell-size of $\Delta x_{min}/c = 4.4414 \cdot 10^{-4}$. Again, both geometry- and flow-based adaptive refinements (AMR) are

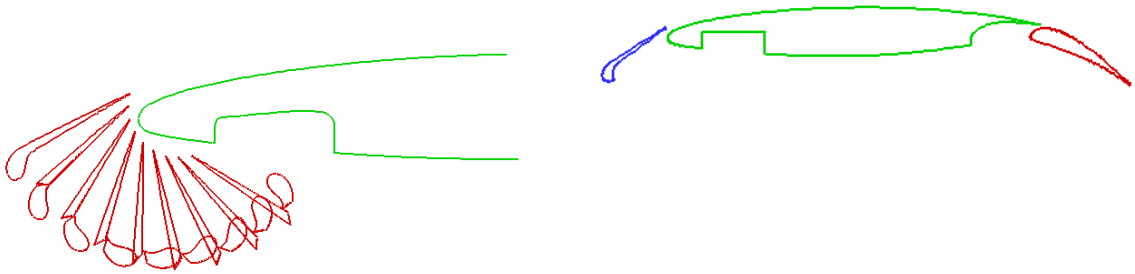

(a) Krueger deployment. (b) Full extended position.

Figure 9. Krueger-flap configuration.

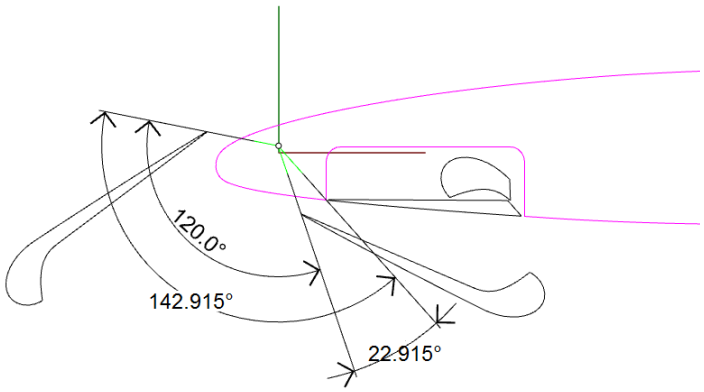

Figure 10. Krueger-flap deployment: geometry simplifications.

applied.

The following numerical simulation deals with the simple rigid body motion (RBM) due to the Krueger-flap deployment. It consists of a clockwise $2D$ rotation around the hinge point shown in figure 10 at a constant rotation speed of $\dot{\theta} = 142.915\, deg/sec$. The full extension occurs in $1\, sec$.

Due to the highly separated flow, the time-accurate simulation starts from an unsteady solution (rather than a steady one) obtained by fixing the Krueger rotation at $\theta = 22.915°$ and running 802 time-steps with $\Delta t^+ = 1.7 \cdot 10^{-2}$ ($\Delta t = 2 \cdot 10^{-4}\, sec$) till reaching $t^+ = 13.634\, CTUs$ ($t = 0.1604\, sec$). After that, the Krueger begins to rotate till reaching the full extended position of $\theta = 142.915°$ at $t^+ = 85$ ($1\, sec$). Note that, the adopted time-step guarantees $CFL^{max}_{body} < 1$.

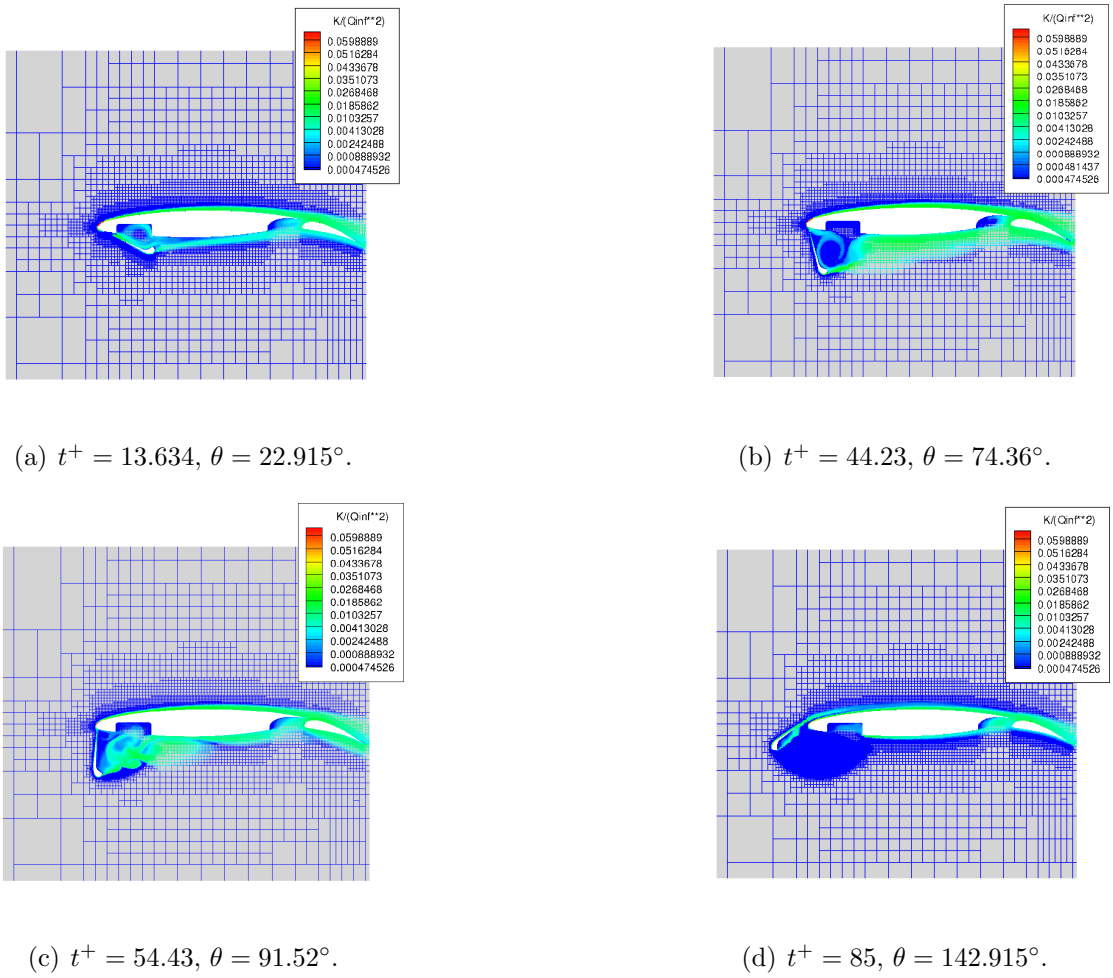

(a) $t^+ = 13.634$, $\theta = 22.915°$.

(b) $t^+ = 44.23$, $\theta = 74.36°$.

(c) $t^+ = 54.43$, $\theta = 91.52°$.

(d) $t^+ = 85$, $\theta = 142.915°$.

Figure 11. Krueger-flap deployment. $Mach = 0.15$, $Re_\infty = 2 \cdot 10^6$. Dynamic AMR mesh colored by the dimensionless turb. kinetic energy.

The figure 11 shows local views of the AMR mesh colored by the dimensionless turbulent kinetic energy and for different rotation angles. As expected, a flow separation occurs downstream the Krueger and extends along the main lower-side. It involves the bay with a complex mixing that influences the belly flow as well as the flap zone.

As the Krueger rotates, the flow-mixing enlarges till reaching the typical bluff-body wake whose extension is maximum when the wall is nearly perpendicular to the flow $\theta = 75.8°$ at $t^+ = 45$ (t=0.53 sec). After that, the wake-region reduces and the vorticity content of the belly flow appears less significant. As desired, the fully deployed position energizes the air on the main upper-surface.

At each times-step, the pre-processor tags the solid walls and refines the mesh where needed. The dynamic IB-modelling assures the consistent energy transfer between Lagrangian and Eulerian markers and the respect of wall BCs.

The plots shown in figure 12 compares the transient loads obtained by using two different time-steps of $\Delta t = 2 \cdot 10^{-4}\, sec$ and $\Delta t = 2 \cdot 10^{-5}\, sec$.

As expected, the lift time-histories exhibit the drop due to the large wake behind

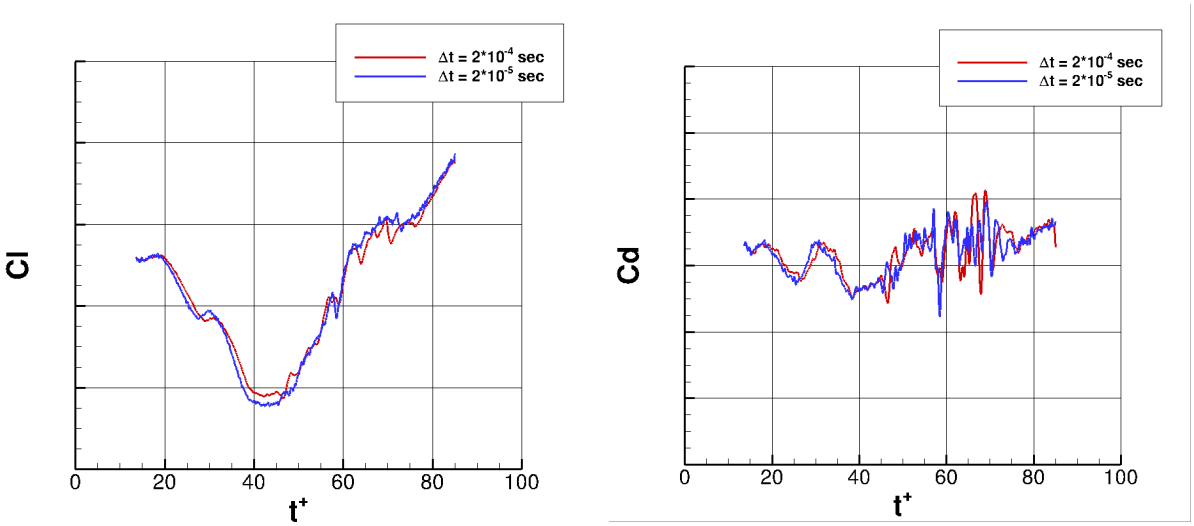

(a) Lift coeff.

(b) Drag coeff.

Figure 12. Krueger-flap deployment. $Mach = 0.15$, $Re_\infty = 2 \cdot 10^6$. Loads' time-histories: $\Delta t = 2 \cdot 10^{-4}\, sec$ red-colored solid-line, $\Delta t = 2 \cdot 10^{-5}\, sec$ blue-colored solid-line.

the Krueger and the progressive recovery towards the extra lift at the full extended position. The two curves are very similar and almost overlapped. However, the lift drop is more pronounced and the curve appears noisier as time-step decreases.

Analogously, the transient drag is not influenced by the time-step refinement whose major effect is an increase in spurious oscillations. The latter does not surprise as the time-step is decreased by keeping the cell-size constant.

5.3. Slat-main-flap deployment

The geometry is the $DLR - F15$ multi-element high-lift airfoil[39]. It is a cut profile through a $3D$ wing belonging to a transonic large single aisle transport aircraft.

The airfoil consists of a slat, a main element and a flap, which is leading-edge normalized with the sweep angle of the reference wing.

The design flow conditions are $Mach = 0.15$ and $Re_\infty = 7 \cdot 10^6$ referred to the airfoil reference length of $c = 1.0\, m$. The suggested angle of incidence is $\alpha = 10°$.

The two-dimensional computational domain spans $30c \times 30c$ away from the surface and the Cartesian mesh counts a variable number of $O(10^5)$ cells with a minimum cell-size of $\Delta x_{min}/c = 4.8828 \cdot 10^{-4}$. Both geometry- and flow-based refinements are applied. The deployment deals with a simple $2D$ counterclockwise rotation of the slat at a constant rotation speed of $\dot{\theta} = -1.8667\, deg/sec$. At the same time, the flap translates and rotates following a prescribed deployment-law. The complete motion occurs in a time-range of $15\, sec$. Local views of the AMR mesh at different instants of time are shown in figure 13 along with the instantaneous contour map of dimensionless turbulent kinetic energy.

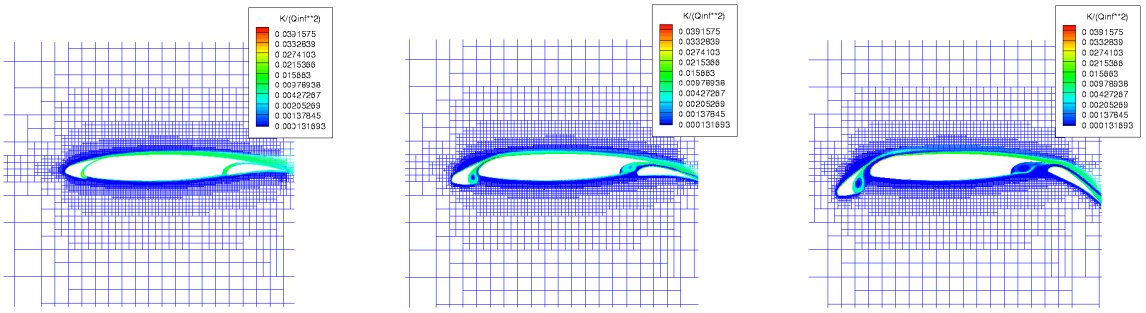

(a) $t^+ = 100$. (b) $t^+ = 400$. (c) $t^+ = 750$.

Figure 13. Flap-slat deployment. $Mach = 0.15$, $Re_\infty = 7 \cdot 10^6$. Dynamic AMR mesh colored by the dimensionless turb. kinetic energy at fully deployment position $t^+ = 750$.

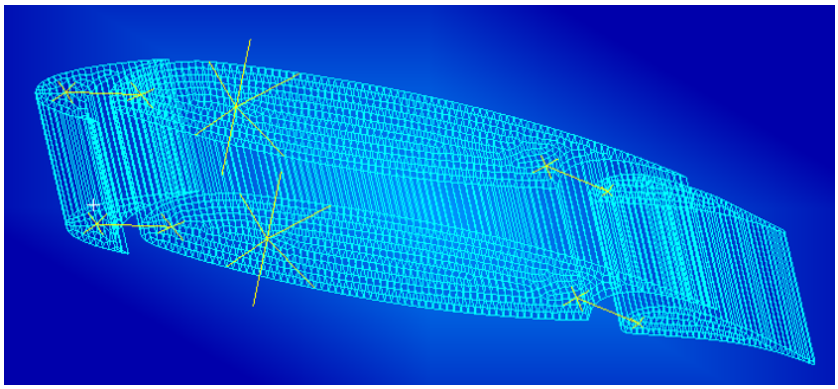

Figure 14. Local view of the quasi-$2D$ FEM model.

At fully retracted position, the flow field is initialized by using a converged steady RANS solution. The complete geometry deployment is obtained after running $750\,CTUs$. A non-dimensional time-step of $\Delta t^+ = 2.5{\cdot}10^{-2}$ ($\Delta t = 5{\cdot}10^{-4}\,sec$) is used. It guarantees that the CFL based on the maximum wall velocity is less than one. The first deployment phase is characterized by an almost steady flow. After $100\,CTUs$ ($2\,sec$), two recirculating zones appear in the slat and main coves due to geometric concavities. As the slat and flap open, the two steady bubbles enlarge. The latter, however, do not cause large separations on the main and flap surfaces. In particular, the URANS model estimates an almost continue loads' increase throughout the deployment phase as it will be shown afterwards.

The first $2D$ simulation considers only the rigid body motion (RBM) due to the roto-translations of slat and flap without considering aeroelastic effects. At each time-step the mesher tags the new surface position and splits the IB cells marking them as solid or fluid by considering their mutual position w.r.t. the moving object. The MLSQ procedure reconstructs, in space and time, the flow-state vector at 'fresh' cells that emerge towards the fluid region.

The transient load coefs. (referred to $A_{ref} = 1\,m^2$) are shown in figure 15 and

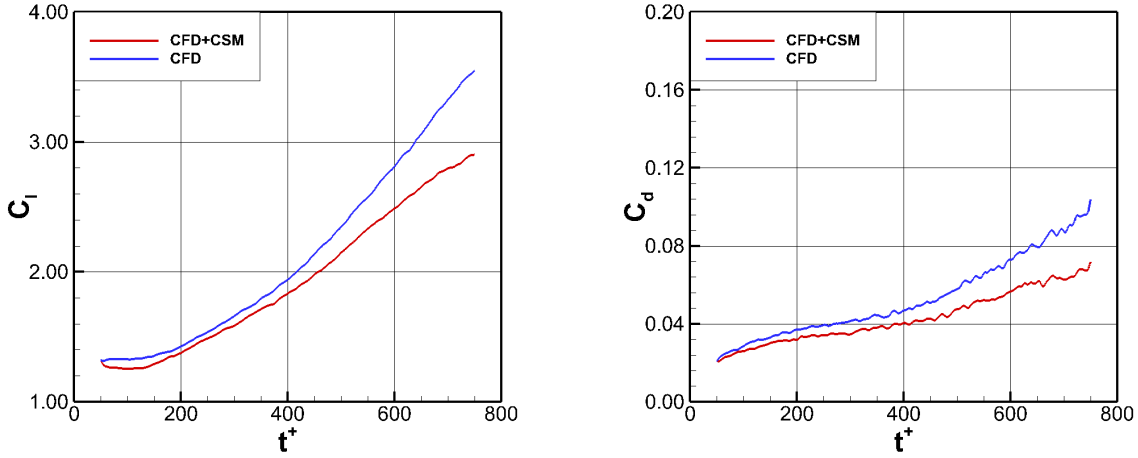

(a) Lift coeff.

(b) Drag coeff.

Figure 15. Flap-slat deployment. $Mach = 0.15$, $Re_\infty = 7 \cdot 10^6$. Loads' time-histories.

blue-colored. As anticipated above, the two recirculating zones are confined to the slat and main coves and have little influence on the regular flow patterns around the main and flap surfaces. This explains why, at $\alpha = 10°$, the high-lift device is able of doubling the $2D$ lift coefficient.

The second computation considers the elastic behavior of the geometry and applies a loose coupling between fluid- and structural-dynamics during the whole deployment phase. The FEM model is a $2.5D$ structure with only one-element width along the span as shown in figure 14. It represents a rod from steel with cross section radius of $0.05\,m$.

The body structures (slat, main and flap) are modelled with solid hexa- and penta-elements. The connection slat-to-main and flap-to-main are made from simple beam elements with $50mm$ radius. To simplify, the beam length is self-adjustable and follow the motion of its end-nodes. In addition, auxiliary beams are introduced to stabilize the model. The latter is arbitrarily fixed at the 25% of the chord. The material is assumed to be steel for both solid and beam elements. A simplified model is considered having one cell width of $1m$ in the span. The connections as well as model constraints are placed at the span-ends of the model.

The loose FSI coupling is obtained by applying a linear and static structural modelling at each time-step following the staggered scheme shown in figure 4. In particular, CFD starts its computation at t^j_{CFD} and delivers the surface loads f_i to CSM. The interface makes data interpolation, mapping and loads transfer for CSM. Since the CFD simulations are two-dimensional, the pressure load is propagated uniformly in the span. Then, the Nastran static solver computes the structural model with stiffness S_i at time $t^i_{CSM} = t^j_{CFD}$. The middle section is used as a two-dimensional representation of the structural deformation. The displacements $\widehat{x}_i$ are transferred back to CFD that continues its computation.

The current FSI process is driven by the unsteady flow solver and it has been

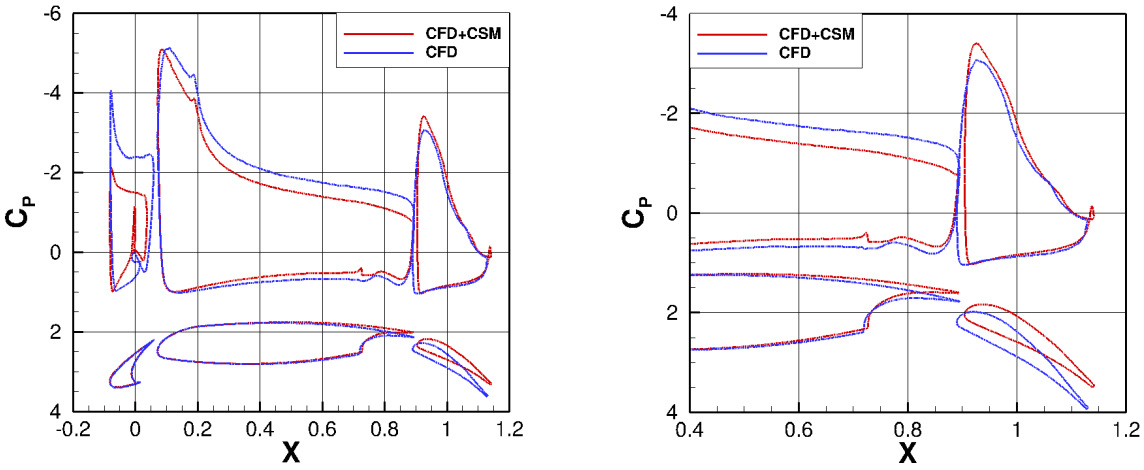

(a) Global view. (b) Local view.

Figure 16. Flap-slat deployment. $Mach = 0.15$, $Re_\infty = 7 \cdot 10^6$. Pressure coeff. and modified shapes due to aeroelastic loads at $t^+ = 750$ ($15\,sec$).

running for $30,000$ time-steps with $\Delta t^+_{FSI} = \Delta t^+_{CFD}$. An implicit loop verifies the loads' convergence by checking that $|\Delta C_l|_\infty < 5 \cdot 10^{-3}$ so as to guarantee a maximum number of $2 \div 5$ sub-iterations.

The aeroelastic loads are shown in figure 15 and red-colored. In particular, the lift coefficient slightly decreases around $t^+ = 100$ ($t = 2\,sec$) mainly due to a flap deformation in the positive z-direction. Later, it increases but its growth rate is less than the rigid case. When the device is fully deployed, the lift coefficient is decreased by nearly 13% w.r.t. the rigid case. Due to aeroelastic effects, the transient drag increases but slower than the RBM case and results in a drag drop of nearly 30% in the fully open position.

The high-lift loads cause visible changes to the trailing-edge of the main component. Partial rotation, translation and deformation occur for the flap itself as shown in figure 16-a. The comparison of pressure distributions clarifies the reasons behind the lift drop at the fully deployed position. As expected, the changes occurring in the flap area (figure 16-b) cause local pressure variations de-facto modifying the global loads.

On the whole, the loose FSI coupling estimates that the device deployment causes a lift drop while the efficiency slightly increases.

The advantage in terms of simulation turn-around time is clear. For example, the time required to generate automatically $O(10^5)$ flow-adapted Cartesian cells around the three-element airfoil is about 10 seconds. Besides, this occurs only at the first meshing-step. The CPU-time decreases to roughly $4\,sec$ if a 'local' mesh update is required due to body motions/deformations at each time-step.

The above numbers would say nothing if not put in a three-dimensional context. In general, the man-power required to build-up a multi-block structured or unstructured mesh of 20M cells around a three-dimensional configuration (of medium complexity)

takes 15 to 30 days. Besides, the meshing process is carried out almost entirely by hand and requires expert technicians. On the contrary, the same number of Cartesian cells are generated automatically in about 20 minutes. Assuming that the CPU-time per iteration per cell is more or less the same among flow solvers, it turns out that the present method speeds up the simulation process of one order of magnitude, at least for fixed geometries.

One of the main issues encountered during the simulation process is a local violation of the $CFL_{body} < 1$ condition somewhere in the emerging cells. The above constrain obliges to pay attention to an a priori estimate of the maximum allowed time-step. About the current three-element deployment, it is sufficient a slight decrease of the time-step to obtain a stable FSI process (once fixed the desired cell-size). However, this is not possible in case of flows driven by large deformations. In those cases, the time-step has to be tuned dynamically.

6. Conclusions

An immersed boundary method is developed to allow the simulation of compressible, inviscid or viscous flows around moving/deforming objects. A hybrid Lagrangian-Eulerian approach considers the motion of bodies through a fixed Cartesian mesh.

The data management is modified to account for 'fresh' and 'dead' cells during the dynamic meshing and the tagging phases. A MLSQ procedure allows accurate and consistent space and time reconstructions in those cells that do not have a time-history. A dynamic IB-model considers the body motions by means of proper Lagrangian markers and satisfies local BCs there. The model uses the surface velocities to account for rigid roto-translations and/or local wall deformations.

The results obtained for the oscillating airfoil are in line with other numerical data from literature and demonstrate the applicability of the method in case of objects moving with prescribed rigid laws.

The method is applied to the rigid deployment of a Krueger-flap device and the results are discussed in terms of aerodynamic performance by monitoring the transient loads during the Krueger rotation.

An FSI interface is developed to drive the solution sequence between the IB-method and a CSM-solver in a fully automatic mode. A loose coupling, based on a staggered sequence, is applied to the deployment of a three-element airfoil and a $2.5D$ transient solution is computed in a short turnaround time.

Of course, the final aim is to simplify and automate the numerical analysis of the Krueger-flap deployment. Nevertheless, this technology has the potential to be exploited for studying different aeroelastic problems, such as the wing-buffeting, the opening of landing-gears and doors, just to cite few.

7. Future work

The loose FSI coupling is object of continuous upgrading for allowing fully three-dimensional aeroelastic analyses. In particular, the dynamic Cartesian method is being modified to speed-up the tagging as well as the meshing algorithms.

A tight non-linear FSI coupling is under development. Once available, it will be used for computing a full-span Krueger-flap deployment for which the wind-tunnel measurements will be available soon.

Acknowledgments

The research activity is supported by the European Community's Horizon 2020 Programme under grant agreement $N°769088$ - UHURA.

References

[1] Tezduyar, T. E., "Finite Element methods for flow problems with moving boundaries and Interfaces," *Archives of Computational Methods in Engineering*, Vol. 8, 2001, pp. 83–130.

[2] Liao, W., Cai, J., and Tsai, H., "A multigrid overset grid flow solver with implicit hole cutting method," *Computer Methods in Applied Mechanics and Engineering*, Vol. 196, 2007, pp. 1701–1715.

[3] Cornell, B. S. H. and Yue, D. K. P., "Falpping Dynamics of a Flag in a Uniform Stream," *Journal of Fluid Mechanics*, Vol. 581, 2007, pp. 33–67.

[4] Renard, N. and Wild, J., "Unsteady simulation of the flow during the deployment of High-Lift systems," *European Congress on Computational Methods in Applied Sciences and Engineering, ECCOMAS* 2012, Vienna, Austria, 2012, pp. 1–19.

[5] Cinquegrana, D. and Vitagliano, P., "Non-linear panel instabilities at high-subsonic and low supersonic speeds solved with strongly coupled CIRA FSI framework," *International Journal of Non-Linear Mechanics*, Vol. 129, 2021, pp. 103643.

[6] Cai, J., Tsai, H., and Liu, F., "A parallel viscous flow solver on multi-block overset grids," *Computer and Fluids*, Vol. 35, 2006, pp. 1290–1301.

[7] Takahashi, S., Monjugawa, I., and Nakahashi, K., "Unsteady Flow Computations around Moving Airfoils by Overset Unstructured Grid Method," *Trans. Japan Soc. Aero. Space Sci.*, Vol. 51, 2008, pp. 78–85.

[8] Gilmanov, A. and Sotiropoulos, F., "Hybrid CartesianImmersed Boundary Method for Simulating Flows with $3D$, Geometrically Complex, Moving Bodies," *Journal of Computational Physics*, Vol. 207, No. 2, 2005, pp. 457–492.

[9] Uhlmann, M., "An immersed boundary method with direct forcing for the simulation of particulate flows," *Journal of Computational Physics*, Vol. 209, 2005, pp. 448–476.

[10] Yang, X., Zhang, X., Li, Z., and He, G.-W., "A smoothing technique for discrete delta functions with application to immersed boundary method in moving boundary simulations," *J. Comp. Physics*, Vol. 228, 2009, pp. 7821–7836.

[11] Vanella, M. and Balaras, E., "A moving-least-square reconstruction for embedded-boundary formulations," *Journal of Computational Physics*, Vol. 228, 2009, pp. 6617–6628.

[12] Bopp, M. S. and Ruffin, S. M., "Development of a Fluid-Structure Interaction Framework Using Unstructured Cartesian CFD Methods," *34th AIAA Applied Aerodynamics Conference*, Washington, D.C., USA, 2016, pp. 1–24, AIAA Paper 2016–3871.

[13] de Tullio, M., , and Pascazio, G., "A Moving-Least-Squares Immersed Boundary Method for

Simulating the Fluid-Structure Interaction of Elastic Bodies with Arbitrary Thickness," *J. Comp. Physics*, Vol. 325, 2016, pp. 2001–225.

[14] Schneiders, L., Günther, C., Meinke, M., and Schröder, W., "An efficient conservative cut-cell method for rigid bodies interacting with viscous compressible flows," *Journal of Computational Physics*, Vol. 311, 2016, pp. 62–86.

[15] Peskin, C. S., "Flow Patterns Around Heart Values: a Numerical Method," *Journal of Computational Physics*, Vol. 10, 1972, pp. 252–271.

[16] Liao, C. C., Chang, Y. W., Lin, C. A., and McDonough, J. M., "Simulating flows with Moving Rigid Boundary using Immersed-Boundary Method," *Computer and Fluids*, Vol. 39, 2010, pp. 152–167.

[17] Yang, J. and Balaras, E., "An embedded-boundary formulation for large-eddy simulation of turbulent flows interacting with moving boundaries," *J. Comp. Physics*, Vol. 215, 2005, pp. 12–14.

[18] Capizzano, F., "Automatic generation of locally refined Cartesian meshes: data management and algorithms," *International Journal for Numerical Methods in Engineering.*, Vol. 113, No. 5, 2018, pp. 789–813.

[19] Capizzano, F., Alterio, L., Russo, S., and de Nicola, C., "A hybrid *RANS-LES* Cartesian method based on a skew-symmetric convective operator," *Journal of Computational Physics*, Vol. 390, 2019, pp. 359–379.

[20] Kok, J. C., Oskam, B., and van der Ven, H., "Extra-large eddy simulation of massively separated flows," *Proceeding of the 42nd AIAA Aerospace Sciences Meeting and Exhibit*, Reno, Nevada, 2004, pp. 1–12, *AIAA* Paper 2004–264.

[21] Kok, J. C., "Resolving the Dependence on Free-Stream Values for the $\kappa - \omega$ turbulence model," *AIAA J.*, Vol. 38, No. 7, 2000, pp. 1292–1295.

[22] Ham, F. E., Lien, F. S., and Strong, A., "A Cartesian Grid Method with Transient Anisotropic Adaptation," *Journal of Computational Physics*, Vol. 179, 2002, pp. 469–494.

[23] Mavriplis, D. J., "Revisiting the Least-squares Procedure for Gradient Reconstruction on Unstructured Meshes," NIA Report 2003-06, NASA, 2003.

[24] Jameson, A., "Time-Dependent Calculations Using Multigrid, with Application to Unsteady Flows past Airfoils and Wings," *Proceeding of the 10th Computational Fluid Dynamics Conference*, Honolulu, HI, U.S.A., 1991, pp. 1–14, *AIAA* Paper 91–1596.

[25] Melson, N. D. N., Sanetrik, M. D., and Atkins, H. L., "Time-Accurate Navier Stokes Calculations with Multigrid Acceleration," *Proceeding of the 6th Copper Mountain Conference on Multigrid Methods*, NASA Conference Publication, 1993, pp. 423–437.

[26] Capizzano, F., "Turbulent Wall Model for Immersed Boundary Methods," *AIAA J.*, Vol. 49, No. 11, 2011, pp. 2367–2381.

[27] Dadone, A. and Grossman, B., "Further Developments in the Three-Dimensional Cartesian-Grid Ghost-Cell Method," *44th AIAA Aerospace Science Meeting and Exhibit*, Reno, Nevada, USA, 2006, pp. 1–20, AIAA Paper 2006–1085.

[28] Tseng, Y. H. and Ferziger, J. H., "A ghost-cell immersed boundary method for flow in complex geometry," *Journal of Computational Physics*, Vol. 192, 2003, pp. 593–623.

[29] de Palma, P., de Tullio, M., Pascazio, G., and Napolitano, M., "An immersed boundary method for compressible viscous flows," *Computers and Fluids*, Vol. 35, 2006, pp. 693–702.

[30] de Tullio, M., de Palma, P., Iaccarino, G., Pascazio, G., and Napolitano, M., "An Immersed Boundary Method for Compressible Flows using Local Grid Refinement," *J. Comp. Physics*, Vol. 225, 2007, pp. 2098–2117.

[31] Capizzano, F., "Coupling a Wall Diffusion Model with an Immersed Boundary Technique," *AIAA J.*, Vol. 54, No. 2, 2016, pp. 2367–2381.

[32] Lee, J., Kim, J., Choi, H., and Yang, K.-S., "Sources of Spurious Force Oscillations from an Immersed Boundary Method for Moving-Body Problems," *Journal of Computational Physics*, Vol. 230, No. 7, 2011, pp. 2677–2695.

[33] Seo, J. H. and Mittal, R., "A sharp-interface immersed boundary method with improved mass conservation and reduced spurious pressure oscillations," *Journal of Computational Physics*, Vol. 230, No. 19, 2011, pp. 7347–7363.

[34] Murman, S. M., Aftosmis, M. J., and Berger, M. J., "Simulations of 6-DOF Motion with a Cartesian Method," *41st AIAA Aerospace Sciences Meeting*, Reno, Nevada, USA, 2003, pp. 1–18, AIAA Paper 2003–1246.

[35] "ALGLIB - Numerical analysis library, 1999-2000." 2020.

[36] Venkatakrishnan, V. and Mavriplis, D., "Implicit method for the computation of unsteady flows on unstructured grids," *Journal of Computational Physics*, Vol. 127, No. 2, 1996, pp. 380–397.

[37] Landon, R., "Compendium of unsteady aerodynamic measurements," Ar–702, AGARD Working Group 702, 1982.

[38] Kirshman, D. J. and Liu, F., "Flutter prediction by an Euler method on non-moving Cartesian grids with gridless boundary conditions," *Comput. Fluids*, Vol. 35, 2006, pp. 571–586.

[39] Wild, J., "Mach and Reynolds Number Dependencies of the Stall Behavior of High-Lift Wing-Sections," *AIAA Journal*, Vol. 50, 2013, pp. 1202–1216.

[40] Ciobaca, V. and Dandois, J., "High Reynolds Number High-Lift Airfoil Testing with Flow Control," *35th AIAA Applied Aerodynamics Conference*, Denver, Colorado, USA, 2017, pp. 1–20, AIAA Paper 2017-3245.